ЖЭТФ, 2012, том 141, вып. 6, стр. 1167–1182

RING-SHAPED SPATIAL PATTERN OF EXCITON LUMINESCENCE FORMED DUE TO THE HOT CARRIER TRANSPORT IN A LOCALLY PHOTOEXCITED ELECTRON–HOLE BILAYER

A. V. Paraskevov [a,b*]

[a] *National Research Center "Kurchatov Institute" 123182, Moscow, Russia*

[b] *Department of Physics, Loughborough University Loughborough LE11 3TU, United Kingdom*

Received September 7, 2011

A consistent explanation of the formation of a ring-shaped pattern of exciton luminescence in GaAs/AlGaAs double quantum wells is suggested. The pattern consists of two concentric rings around the laser excitation spot. It is shown that the luminescence rings appear due to the in-layer transport of hot charge carriers at high photoexcitation intensity. Interestingly, one of two causes of this transport might involve self-organized criticality (SOC) that would be the first case of the SOC observation in semiconductor physics. We test this cause in a many-body numerical model by performing extensive molecular dynamics simulations. The results show good agreement with experiments. Moreover, the simulations have enabled us to identify the particular kinetic processes underlying the formation of each of these two luminescence rings.

1. INTRODUCTION

Non-equilibrium collective effects in the exciton and exciton–polariton systems in semiconductor heterostructures are a subject of intensive studies [1–26]. A particular attention has been focused on the beautiful phenomenon discovered experimentally in the system of interwell excitons in GaAs/AlGaAs double quantum wells (QWs) [6]: at sufficiently high excitation intensity, a local photoexcitation of electrons (e) and holes (h) above the exciton resonance gives rise to a macroscopic ring-shaped pattern of spatial distribution of the exciton luminescence. The radius of the pattern can be varied in a wide range by tuning external parameters such as the excitation intensity or gate voltage. Remarkably, at sub-Kelvin lattice temperatures the external ring of the stationary pattern exhibits a sharp fragmentation, which could be the signature of a non-equilibrium macroscopic quantum effect.

Understanding the nature of the ring-shaped pattern requires building a many-body model that captures local generation of electron–hole pairs and their spatial dynamics accompanied by the processes of formation and recombination of excitons. If the exciton lifetime is sufficiently long, the spatial dynamics of the excitons should also be considered.

The first theoretical explanation that met these requirements was based on the diffusive transport model (DTM) applied to the locally photogenerated holes and equilibrium electrons, which were initially distributed uniformly in the quantum-well plane [13, 14, 16, 17, 24]. The overlapping region for the hole and electron spatial distributions apparently gave rise to the ring of exciton luminescence.

However, this explanation has a lot of evident shortcomings [27]. For example, if the same number of photogenerated electrons is added to the model (in principle, they must be added to maintain the electroneutrality), then the ring of exciton luminescence can disappear due to the exciton formation term, which is simply proportional to the product of the electron and hole densities. (If these densities decrease monotonically from the excitation spot center, then the luminescence intensity would apparently follow them.) More specific shortcomings can be found in Appendix A.

In this paper, a novel consistent explanation of the ring-shaped pattern formation is given. The main idea is that an essential in-plane electric field occurs in the

*E-mail: avp.workbox@yandex.ru

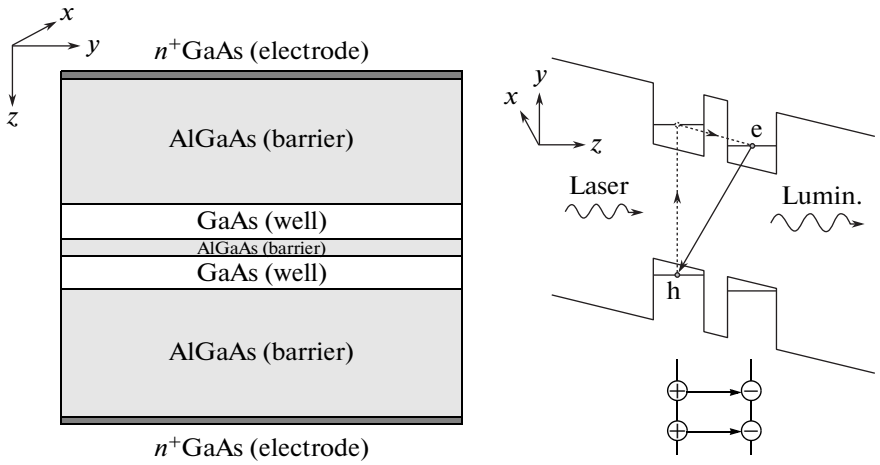

Fig. 1. Left: Schematic of a double quantum well (DQW). The DQW structure is bordered by highly-doped GaAs layers that serve as external electrodes forming a plane capacitor. In the experiments [6, 13, 24], the widths of the layers between the electrodes are (200 nm) (8 nm) (4 nm) (8 nm) (200 nm), respectively. Right: (Top) Schematic of the DQW energy profile along the "growth" axis (z axis) when a voltage is applied between the external electrodes (it results in a linear bias of the profile) and interwell exciton formation (arrows show the path of a photoexcited electron). (Bottom) Interwell excitons as co-directed classical dipoles

excitation spot region at sufficiently high excitation power. This field strongly affects the spatial dynamics of the photogenerated electrons and holes. (We do not consider any equilibrium carriers at all.) We show that there are contributions to the electric field from two quite different physical processes. Essentially, due to one of these contributions, the ring-shaped pattern formation could be understood in the paradigm of self-organized criticality (SOC) [28]. To test the contribution, we have performed extensive molecular dynamics simulations. They have shown that this contribution alone is quite enough for a detailed qualitative explanation of the ring-shaped pattern. (However, this paper does not consider the transition to the SOC regime. The parameters for the simulations have been chosen to be in this regime from the very beginning.)

This paper is organized as follows. Further in this section, we introduce some essential properties of double quantum wells and interwell exciton formation, some experimental results we focus on, and the formulation of the problem to be studied. In Sec. 2, we suggest two qualitative explanations ("scenarios") for the ring-shaped pattern formation and make the corresponding estimates. Section 3 describes a many-body dynamical model and conditions of the molecular dynamics simulations performed to investigate the second scenario in more detail. Section 4 contains the results of the simulations. Section 5 is conclusion and discussion. Finally, Sec. 6 consists of three Appendices.

The structure of double QWs used in the experiments [6, 13, 24] is shown in Fig. 1 (left). The electron band-gap energy E_{gap} of the "barrier" (B) layers is larger than E_{gap} of the "well" (W) layers (Fig. 1 (right)), and hence GaAs layers form two rectangular potential wells with the depth

$$U_{QW} = \left(E_{gap}\left(B\right) - E_{gap}\left(W\right)\right)/2 \approx 0.4 \text{ eV}.$$

At a moderate occupation of the wells (i. e., when the number of electrons in the GaAs conduction band is not macroscopically large; see the next section for the details), a voltage applied to the external electrodes provides a constant tilt of the DQW potential profile (Fig. 1 (right)). This "gate" voltage V_g is needed to separate electrons and holes in the different wells, facilitating the formation of interwell excitons. The crossover between the interwell and intrawell exciton "ground" states occurs at $V_g \approx 0.3$ V [29]. (Since $V_g > 0.3$ V in the experiments [6, 13, 24], the intrawell excitons are not discussed in what follows.) The stationary laser pumping comes along z axis and is used for the formation of a macroscopic number of photogenerated electron–hole pairs. In the experiments [6, 13, 24], the typical laser power was several hundreds of μW and was focused in a spatial spot of few tens of μm. The pumping energy was well above the exciton resonances, and hence an electron was photoexcited to a high-energy level of the QW near the continuum. Due to the applied gate voltage, the electron can then tunnel to the

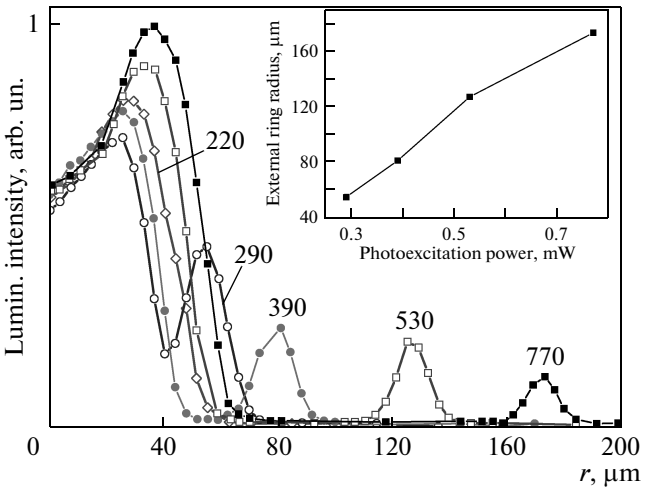

Fig. 2. Experimental curves taken from Ref. [6]: the luminescence intensity of interwell excitons vs the distance r from the excitation spot center at different excitation powers (the numbers near the curves are expressed in μW). The excitation spot radius is about 20 μm. Inset: Dependence of the external ring radius on the excitation power

corresponding QW. (The effective mass of an electron in GaAs is seven times smaller than the mass of a heavy hole, so the tunneling is much more probable for electrons than for holes. We note that the energy of heavy holes is lower than the energy of light ones in GaAs.) The tunneling might also be facilitated by the voltage-induced triangular profile of the barrier. Finally, after a spatiotemporal in-layer relaxation of the charge carriers, the interwell excitons are formed; they live some finite time and then annihilate, giving rise to the photoluminescence (PL) pattern in the QW (xy) plane.

We now turn to the experimental results that we intend to explain (Fig. 2). At a small excitation power, the PL spatial profile practically follows the excitation spot (see the details in [6]). When the excitation power exceeds a certain value, a thick ring of luminescence appears near the edge of the excitation spot. In Ref. [6], it was already seen at the excitation power 220 μW. Hereafter, we call this ring the "internal" ring. Finally, when the excitation power exceeds another critical value (Fig. 2), a thin "external" ring of luminescence appears around the excitation spot and the inner ring. Everywhere in this paper, the words "ring-shaped pattern" mean these two concentric rings.

The formation mechanism of the ring-shaped luminescence pattern is the subject of the research described below. In particular, we pose the following questions. (i) Why does the ring-shaped pattern appear only when the laser excitation power exceeds some critical values? (ii) What are the kinetic processes that underlie the formation of the internal and external rings? (iii) Why does the external ring radius depend strongly on the static gate voltage V_g [30]? (iv) Why does the luminescence of intrawell excitons (i. e., purely "two-dimensional" excitons) not exhibit the ring-shaped pattern [6]?

2. TWO SCENARIOS OF THE RING-SHAPED LUMINESCENCE PATTERN FORMATION

In general, we believe that the ring-shaped PL pattern appears due to the transport of hot uncoupled electrons and holes from the excitation spot at a sufficiently high excitation power. During the spatial spread, the carriers relax in kinetic energy, emitting phonons and can eventually form excitons relatively far away from the excitation spot ("far away" in comparison with the spot radius). We suppose that the hot charge carriers are formed due to (i) in-layer electric fields that occur at high pumping power in the excitation spot region and (ii) high mobilities of the charge carriers in GaAs. We suggest two particular mechanisms of the electric field occurrence, they are described in detail in Secs. 2.1 and 2.2.

2.1. First scenario: hot carrier transport induced by the external gate voltage

The first scenario concerns the screening of the gate voltage V_g by photogenerated carriers in the excitation spot (Fig. 3) at high excitation power.

The electric induction in the bilayer volume at the laser excitation spot is $\mathbf{D} = \mathbf{E} + 4\pi\mathbf{P}$. Here $\mathbf{E} = E_0\mathbf{e}_z$ is the static uniform electric field generated by V_g and $\mathbf{P}$ is the polarization of the medium. If n is the density of electron–hole pairs in the excitation spot of area S and d is the average distance between the pairs in different wells (i. e., d is the dipole length), then

$$\mathbf{P} = -\frac{(nS)\,(ed)}{Sd}\mathbf{e}_z = -\,(ne)\,\mathbf{e}_z, \quad \mathbf{D} = (E_0 - 4\pi ne)\,\mathbf{e}_z.$$

In the experiments [29], the DQW structure was regarded as an insulator. This means that the condition

$$E_0 \gg 4\pi en, \tag{1}$$

must be satisfied in the excitation spot region. In this case, the gate voltage results in a linear slope of the DQW potential energy profile along the z axis on the value $\delta U\,(z) \approx -eE_0 z$ (Fig. 1 (right)).

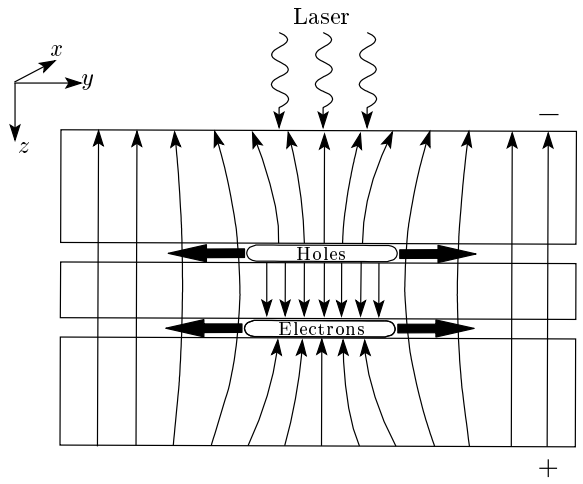

Fig. 3. Schematic of the electric field distribution along the growth axis (z axis) of the DQW structure in the vicinity of laser excitation spot at high excitation power. (It is supposed that the excitation spot is far away from the DQW edges and external contacts.) In the spot region (ovals in the center), the static electric field induced by the external gate voltage is curved due to the presence of a macroscopically large number of photogenerated charge carriers. The horizontal projections of the field cause in-layer transport (shown by thick arrows) of the carriers from the excitation spot

However, at typical values $V_g \approx 1$ V and $n \sim$ $\sim 10^{10}$ cm^{-2} [29], we obtain $eE_0 \approx eV_g/2L \sim$ $\sim 10^4$ eV/cm, where $L = 200$ nm is the width of external barrier of the DQW structure (Fig. 1 (left)), and $4\pi ne^2 \sim 10^4$ eV/cm. So at the expected densities $n \sim$ $\sim 10^{11}$–10^{12} cm^{-2} in the excitation spot at high pumping power, condition (1) is therefore not satisfied there. This means that the z-axis component of the resulting field E_z is essentially dependent on z in the excitation spot region. More importantly, in this case there exists an in-plane component E_r of the electric field that pushes both electrons in one layer and holes in another layer away from the excitation spot (Fig. 3).

2.2. Second scenario: hot carrier transport induced by the repulsive in-layer interaction

If the photogenerated electrons and holes do not leave the excitation spot for any reason, then the higher the pumping power P_{ex} is, the higher the carrier densities in the spot. (Because the excitation is off-resonant, the value of the exciton formation time is always larger than the time of energy relaxation of the carriers to reach the exciton transition.) Due to the bilayer geometry, there exists a value of excitation power at which the carrier densities in the spot reach the values when repulsive in-layer Coulomb forces between carriers become stronger than the attractive interlayer force. To be more specific, we estimate the interaction strength in the excitation spot in terms of the dimensionless interaction parameter r_s. At small carrier densities, the interaction in the spot is the dipole–dipole one rather than the Coulomb as in the case of a monolayer. In particular, for an electron (or hole) monolayer,

$$r_s = \frac{e^2/\bar{r}}{\hbar^2/m\bar{r}^2} = \frac{\bar{r}}{a_B} \sim \frac{1}{\sqrt{na_B^2}}, \qquad (2)$$

where $a_B = \hbar^2/me^2$ is the Bohr radius, n is the carrier density in the spot, and $\bar{r} \sim n^{-1/2}$ is the average distance between carriers. (Hereafter, we omit dielectric constant in the formulas unless making numerical estimates.) Thus, for a monolayer, an increase in the density n leads to a decrease in the interaction. However, in the case of an electron–hole (e–h) bilayer at $\bar{r} > d$, where d is the interlayer distance, the interaction is dipole–dipole: $U = e^2d^2/\bar{r}^3$ rather than $e^2/\bar{r}$. This leads to

$$r_s = \frac{U}{\hbar^2/m\bar{r}^2} = \frac{d^2}{\bar{r}a_B} \sim \frac{d}{a_B}\sqrt{nd^2}, \qquad (3)$$

where $n < n_c \lesssim d^{-2} \sim 10^{12}$ cm^{-2} at $d \sim 10^{-6}$ cm [29]. It follows that in this case the interaction increases in accord with the densities. At $n = n_c$ (which corresponds to some critical excitation power $(P_{ex})_c$) the character of the interaction changes: the repulsive in-layer interaction becomes dominating and, moreover, one should effectively put $n = 0$ in estimate (2), i. e., the repulsive interaction becomes huge. This leads to the appearance of in-layer electric fields ejecting the electrons and holes from the excitation spot region. Then the e–h densities in the spot grow to the critical values again and the ejection process recurs. There is a direct correspondence between this self-organized ejection, which maintains the critical values of carrier densities in the spot, and the avalanches in the classic sand-pile model of SOC [28, 31].

Because the mobilities of charge carriers in GaAs QWs are very high (up to 10^7 cm^2/V·s for electrons at sub-Kelvin temperatures [32–35]), the initial kinetic energies of some part of the ejected particles can exceed the optical phonon emission threshold. Their relaxation in energy is then so fast that these carriers are likely to form excitons not far away from the excitation spot. In turn, the carriers with kinetic energy less than the optical phonon energy $\hbar\omega_{opt}$ go further. These carriers relax relatively slowly by emitting acoustic phonons. In GaAs, $\hbar\omega_{opt} \approx 37$ meV, and hence the

velocities of the carriers contributing to long-distance transport are less than $v_{max} \sim 10^7$ cm/s. (More details about carrier energy relaxation due to phonon emission can be found in Appendix B.)

In addition, there is an essential difference in mobilities, and in effective masses, for electrons and heavy holes in GaAs [32–34]. This can lead to some difference in in-layer "stream" velocities of electrons and holes. The difference, in turn, would result in a suppression of the attractive interlayer Coulomb force (see Appendix C for the details) until the velocities become small enough due to the acoustic phonon emission. In these conditions the interlayer exciton formation is also suppressed in some range of distances from the excitation spot. (We recall, for example, that the classical scattering cross-section for the Coulomb potential, the Rutherford cross-section, is proportional to V^{-4}, where V is the initial relative velocity at infinite distance.) The suppression leads naturally to the formation of a luminescence ring that would define a circumference of the total luminescence pattern.

Thus, the internal ring of luminescence (Fig. 2) might appear due to the electrons and holes that had emitted optical phonon(s) and then quickly formed excitons. In turn, the external luminescence ring can appear due to the carriers that were below the optical-phonon emission threshold and therefore needed more time (and longer distances) to relax by emitting acoustic phonons.

In general, we suggest that at high photoexcitation power there exists an in-plane electric field E_r that consists of two contributions, "gate-voltage-induced" and "in-layer interaction-induced". Due to high mobilities of charge carriers in GaAs, even a moderate value of E_r results in high initial velocities of the carriers directed outside the excitation spot. Large relative velocities of the ejected electrons and holes lead to a suppression of the interlayer Coulomb attraction between them. This results in the suppression of the exciton formation in some range of distances from the excitation spot. In turn, the formation dynamics of the ring-shaped luminescence pattern can be divided into three stages: (i) radial acceleration of carriers in the excitation spot region due to the in-plane component of the static electric field that appears at relatively high carrier density in the excitation spot and due to the in-layer Coulomb repulsion at high pumping power; (ii) deceleration of unbound carriers due to emission of optical and acoustic phonons and due to the ambipolar electric field ("Coulomb drag"); and (iii) the regime of strong interlayer Coulomb correlations: formation and optical recombination of interlayer excitons.

In what follows, we focus on the second scenario and test it by molecular dynamics (MD) simulations.

3. MOLECULAR DYNAMICS SIMULATIONS: NUMERICAL MODEL

To describe the spatial dynamics of N hot electrons and holes, we use the classical equations of motion

$$m_e^*\ddot{\mathbf{r}}_e^i + \gamma_e\dot{\mathbf{r}}_e^i = \sum_{j\neq i}\frac{e^2(\mathbf{r}_e^i-\mathbf{r}_e^j)}{\left|\mathbf{r}_e^i-\mathbf{r}_e^j\right|^3} - \sum_k \frac{e^2\left(\mathbf{r}_e^i-\mathbf{r}_h^k\right)}{\left[\left(\mathbf{r}_e^i-\mathbf{r}_h^k\right)^2+d^2\right]^{3/2}}, \quad (4)$$

$$m_h^*\ddot{\mathbf{r}}_h^i + \gamma_h\dot{\mathbf{r}}_h^i = \sum_{j\neq i}\frac{e^2(\mathbf{r}_h^i-\mathbf{r}_h^j)}{\left|\mathbf{r}_h^i-\mathbf{r}_h^j\right|^3} - \sum_k \frac{e^2(\mathbf{r}_h^i-\mathbf{r}_e^k)}{\left[(\mathbf{r}_h^i-\mathbf{r}_e^k)^2+d^2\right]^{3/2}}, \quad (5)$$

combined with the conditions of exciton formation and optical phonon emission (see below). Here, vectors $\mathbf{r}_e^i$ and $\mathbf{r}_h^j$ are in-plane positions of ith electron and jth hole ($1 \le i, j \le N$), $m^*_{e(h)}$ is the electron (hole) effective mass, e is the electron charge, and d is the interlayer distance (see Fig. 4).

In addition to the inertia terms, the left-hand sides of Eqs. (4) and (5) contain phenomenological momentum damping terms due to the interaction with acoustic phonons with constants $\gamma_{e(h)} = e/\mu_{e(h)}$, where $\mu_{e(h)}$ is electron (hole) mobility. The dimensionless equations are given by

$$\ddot{\mathbf{r}}_e^i + \dot{\mathbf{r}}_e^i = \sum_{j\neq i}\frac{(\mathbf{r}_e^i-\mathbf{r}_e^j)}{\left|\mathbf{r}_e^i-\mathbf{r}_e^j\right|^3} - \sum_k \frac{\left(\mathbf{r}_e^i-\mathbf{r}_h^k\right)}{\left[\left(\mathbf{r}_e^i-\mathbf{r}_h^k\right)^2+d^2\right]^{3/2}}, \quad (6)$$

$$\ddot{\mathbf{r}}_h^i + c_1\dot{\mathbf{r}}_h^i = \sum_{j\neq i}\frac{c_2(\mathbf{r}_h^i-\mathbf{r}_h^j)}{\left|\mathbf{r}_h^i-\mathbf{r}_h^j\right|^3} - \sum_k \frac{c_2(\mathbf{r}_h^i-\mathbf{r}_e^k)}{\left[(\mathbf{r}_h^i-\mathbf{r}_e^k)^2+d^2\right]^{3/2}}, \quad (7)$$

with the constants $c_1 = m_e^*\mu_e/m_h^*\mu_h$ and $c_2 = m_e^*/m_h^*$. Hereafter, we normalize time by $t_e = \sqrt{\epsilon}m_e^*\mu_e/e$, where ϵ is the dielectric constant of the layers, and all distances by $\xi_e = \sqrt[3]{m_e^*\mu_e^2}$. To estimate the parameters, we use the well-known experimental values for high-quality undoped GaAs/AlGaAs QWs. In particular,

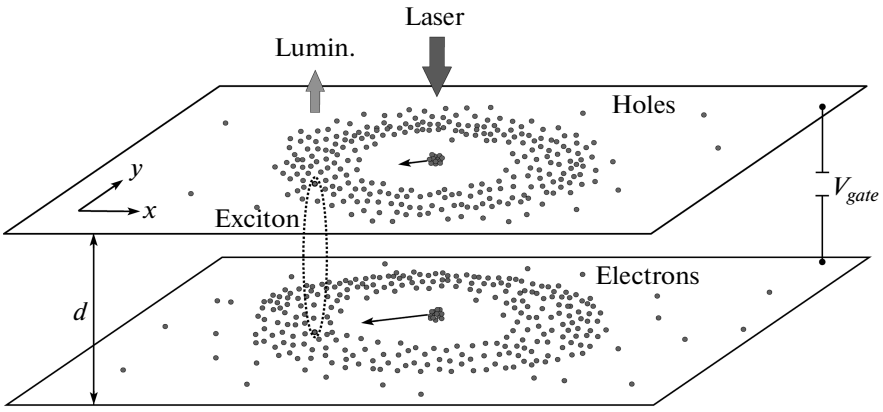

Fig. 4. Qualitative schematic of optically excited electron–hole bilayer. Both stationary laser pumping in the center and spatially distributed luminescence are perpendicular to the layers. The charge separation between the layers postulated in the numerical model is due to the external gate voltage V_{gate}

taking a typical value $\mu_e \sim 10^7$ cm^2/V·s [32, 33] for temperatures $T \lesssim 1$ K, $m_e^* \approx 0.067 m_e$, $m_h^* \approx 0.5 m_e$ (where m_e is the bare electron mass), $\epsilon = 12.8$ and $\mu_h \sim 0.1\mu_e$ [34], we obtain $t_e \sim 10^{-9}$ s, $\xi_e \sim 10^{-4}$ cm, $c_1 \sim 1$, and $c_2 \sim 0.1$.

The optical phonon emission was modeled in the following way: if the kinetic energy of a carrier exceeded the energy of an optical phonon, this last energy was subtracted from the first and the new direction of the carrier velocity became random.

Simulation of laser pumping. Stationary optical pumping of carriers was simulated by generating them in random positions inside the excitation spot of radius r_0 with some generation rate that was modeled in two different ways. In fact, during a MD simulation the time is changed by discrete steps, with the elementary time step Δt. According to the first way [25, 36], the generation rate p was defined as the probability per Δt to create one e–h pair in the excitation spot, so that $p\Delta t < 1$. We name this case the single generation regime (SGR). Alternatively, one can consider the formation of several e–h pairs during Δt. Then the carrier generation rate (CGR) is defined as the number of e–h pairs generated in the excitation spot during the time step Δt. We call it the multiple generation regime (MGR). We note that the results of MD simulations differ essentially in the single and multiple regimes. Indeed, it is intuitively clear that the SGR is likely to correspond to weak pumping, whereas the MGR describes high-power excitation.

The initial velocities of carriers in the excitation spot were also chosen randomly in the intervals $|\dot{\mathbf{r}}_e^i| \le v_0$ and $|\dot{\mathbf{r}}_h^i| \le \eta v_0$, where we took $\eta = 0.5$ in all simulations.

During the spatial dynamics of the carriers, the exciton formation occurred if an electron and a hole were close enough to each other, $|\mathbf{r}_e - \mathbf{r}_h| < a$, where $a(d)$ is a phenomenological in-layer exciton radius, and their relative velocity was smaller than some critical value, $|\dot{\mathbf{r}}_e - \dot{\mathbf{r}}_h| < V_c$ [25] (see also Appendix C). We note that the dependence of the exciton formation rate on the e–h relative velocity is one of the most crucial ingredient for the ring-shaped pattern formation: assuming the absence of that dependence, one always obtains a spatially monotonic decrease of the luminescence outside the excitation spot [25].

To simplify the simulations, we did not consider the exciton dynamics. This means that as soon as an electron and a hole had formed an exciton, their dynamics was no longer considered and the position of the formation event was recorded as a position of photon emission. Qualitatively, this corresponds to zero exciton lifetime.

We note that since both the internal and external ring radii are temperature independent [6, 29], it is not advisable to include temperature (i. e., to add a stochastic force to Eqs. (4) and (5)) into the consideration. In turn, because the low-temperature fragmentation of the external ring [6] apparently depends on the exciton dynamics, we do not expect to observe the fragmentation in the simulation results.

Finally, due to the inevitable restrictions in computational power it was only possible to simulate the dynamics of $N \lesssim 10^4$ interacting particles. For this

reason, we had to modify the values of a, v_0, V_c, d etc. in comparison with realistic values to facilitate the exciton formation. However, it was clearly seen that the closer the values of those model and real parameters were, the better was the correspondence between the MGR simulation results and the experimental ones. We note that the in-plane motion of the carriers was not restricted by any spatial boundaries.

4. MOLECULAR DYNAMICS SIMULATIONS: RESULTS

Some preliminary results for the SGR were published in Ref. [25]. In particular, quasi-1D simulations and the crucial dependence of the ring pattern formation on the critical relative velocity V_c in the exciton formation condition were discussed there. In what follows, some new essential results are described.

4.1. Single generation regime (SGR)

The results of MD simulations of Eqs. (6) and (7) in the SGR for several sets of parameters indicate that there are two qualitatively different pictures. In general, the in-layer distribution $n_{lum}(r)$ of stationary luminescence exhibits a ring-shaped pattern around the excitation spot. But the pattern always contains only one ring. More importantly, the ring can originate by two qualitatively different ways.

According to the first way, the in-layer distributions of electrons and holes are separated from each other and the ring occurs in the region of their overlap (Fig. 5).

The dependence of the ring position on the generation rate p (Fig. 6), which mimics the excitation power, shows that although the luminescence ring intensity increases with p, its position is virtually independent on p (top inset in Fig. 6). This behavior differs from that observed experimentally (Fig. 2), where the radius of the external luminescence ring grows nearly linearly with an increase in the photoexcitation intensity and the growth of the internal ring radius is also quite noticeable. Interestingly, the same behavior, i. e., the independence of the ring position on p, was observed in the quasi-1D case [25].

However, there exists an another way of the ring pattern formation. It was observable at other sets of parameters, in particular, when maximal initial velocities of the carriers, the critical relative velocity V_c, and the distance a were relatively small. We note that the CGR p was taken in the same range of values as previously.

According the second way, the in-layer distributions of electrons and holes practically coincide with each

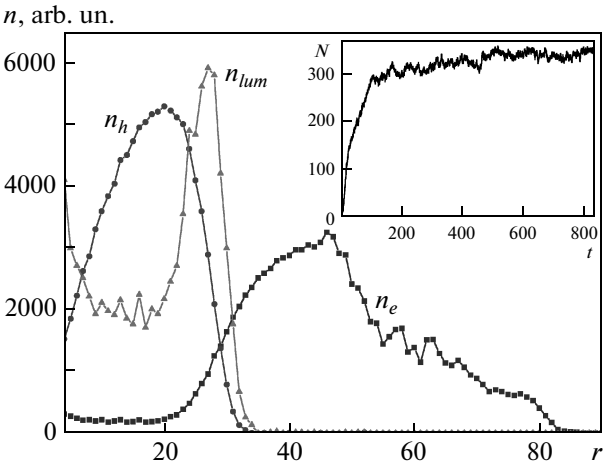

Fig. 5. Stationary in-layer distributions of electrons (n_e), holes (n_h), and luminescence ($n_{lum}(r)$) averaged over time interval $(200, 830)$. Inset: dependence of the total number N of electrons and holes on time t. In a stationary state, the carrier generation rate is balanced by the luminescence rate and $N(t)$ exhibits saturation. Parameters of the simulation: excitation spot radius $r_0 = 4$, $p = 10$, velocity of the optical-phonon emission threshold $v_{opt} = 50$, maximal electron initial velocity $v_0 = 50$, critical relative velocity $V_c = 10$, critical relative distance $a = 0.2$, first and second coefficients in the equations of motion for holes $c_1 = 1$ and $c_2 = 0.25$, $d^2 = 0.01$, time step $\Delta t = 0.0005$

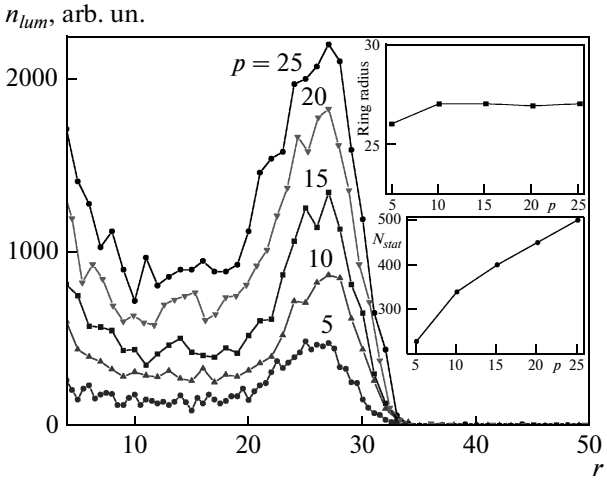

Fig. 6. Dependence of the stationary in-layer luminescence distribution $n_{lum}(r)$ on the generation rate p. Top inset: dependence of the luminescence ring radius on p. Bottom inset: stationary total number N_{stat} of electrons and holes vs p. Parameters of the simulations are the same as in Fig. 5

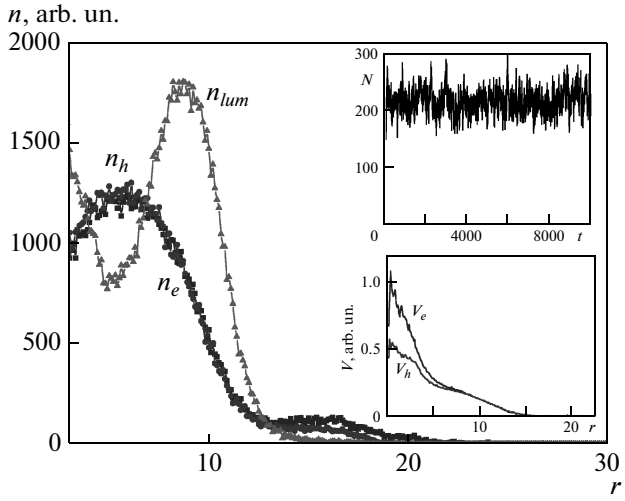

Fig. 7. Stationary in-layer distributions of electrons (n_e), holes (n_h), and luminescence ($n_{lum}(r)$) averaged over time interval (500,10000). Top inset: dependence of the total number N of electrons and holes on time t exhibits a stationary state. Bottom inset: dependence of electron (V_e) and hole (V_h) stream velocities vs the distance r from the excitation spot center. Parameters of the simulation: $r_0 = 3$, $p = 10$, $v_{opt} = 10$, $v_0 = 1$, $V_c = 1$, $a = 0.05$, $c_1 = 1.1$, $c_2 = 0.3$, $d^2 = 0.9$ (the results are essentially the same at smaller d^2), time step $\Delta t = 0.005$

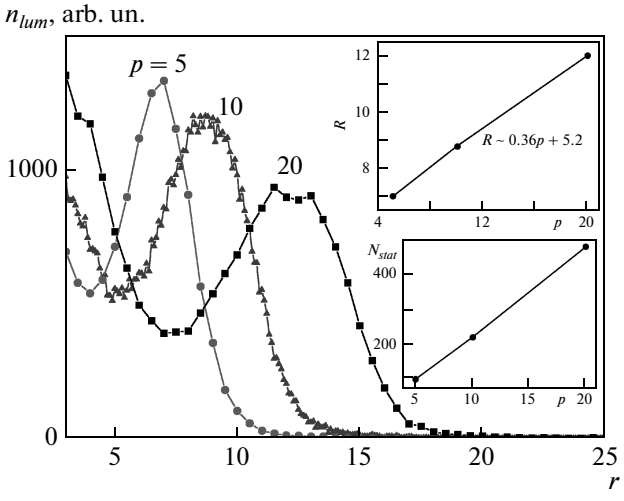

Fig. 8. Dependence of the stationary in-layer luminescence distribution $n_{lum}(r)$ on the generation rate p. Top inset: dependence of the luminescence ring radius R on p. Bottom inset: the stationary total number N_{stat} of electrons and holes vs p. Parameters of the simulations are the same as in Fig. 7

other (Fig. 7). The ring occurs at the outer side of the distributions, where the differences in the carrier densities and velocities are small enough to allow the exciton formation. The dependence of the ring radius on the CGR p (Fig. 8) has shown that, in contrast to the previous case (Figs. 5 and 6), the radius increases linearly with p.

Summarizing the simulation results for the SGR, we conclude that the first way of the ring pattern formation, when electron and hole in-plane distributions are separated and the ring is formed in their overlap region, does not correspond qualitatively to the experimental results [6, 13, 24]. The second way could mimic the experimental situation when the excitation power was such that only the internal luminescence ring was observable. However, the position of the ring in the simulations depends on the pumping rate stronger (linearly) than that of the internal ring (cf. Fig. 2 and Fig. 8) in the experiments [6, 13, 24]. In turn, a nearly linear dependence of the ring radius on the excitation power is typical for the external luminescence ring (Fig. 2), but then the simulations miss the internal ring.

This misfit can indicate that though the parameters of the simulations in the second case are closer to realistic ones, one needs more realistic carrier generation algorithm which would enable us to model high excitation powers and, at the same time, is independent on the MD time step Δt.

4.2. Multiple generation regime (MGR)

In the MGR, the simulations result in much better correspondence with experimental plots (Fig. 2) and, simultaneously, some correspondence with the SGR results ("the second way") can be traced.

First, the MGR results show two concentric rings in the in-layer luminescence pattern: the internal ring has small radius and high intensity and the external ring has relatively large radius and is weaker in intensity (Fig. 9). The in-layer distributions of electrons and holes are similar to those of the above SGR "second way" (Fig. 7), i. e., the distributions practically coincide with each other.

Due to the increase of the effective pumping power in the MGR case, the total number of carriers in the stationary state (inset in Fig. 9) is more than one order of magnitude larger than that in the SGR case. We note that the stationary number of carriers in the excitation spot is very close to the product of the instant CGR ($\Delta N_{spot}/\Delta t = 300$) and the unit time (= 1). This

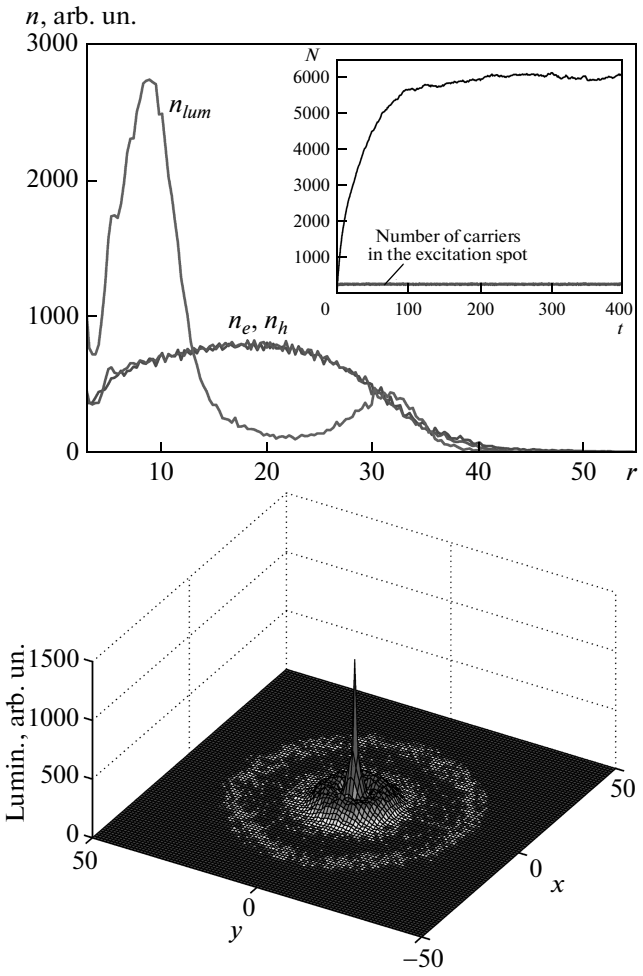

Fig. 9. Top: Stationary in-layer distributions of electrons (n_e), holes (n_h), and luminescence ($n_{lum}(r)$) averaged over the time interval $(100, 400)$. Inset on top: dependence of the total number N of electrons and holes on time t exhibits a stationary regime. Bottom: $3D$ luminescence pattern. Parameters of the simulation: $r_0 = 3$, pumping rate (number of particles generated during the time step Δt in the spot) $\Delta N_{spot} = 3$, $v_{opt} = 10$, $v_0 = 1$, $V_c = 1$, $a = 0.05$, $c_1 = 1.1$, $c_2 = 0.3$, $d^2 = 0.9$, and $\Delta t = 0.01$

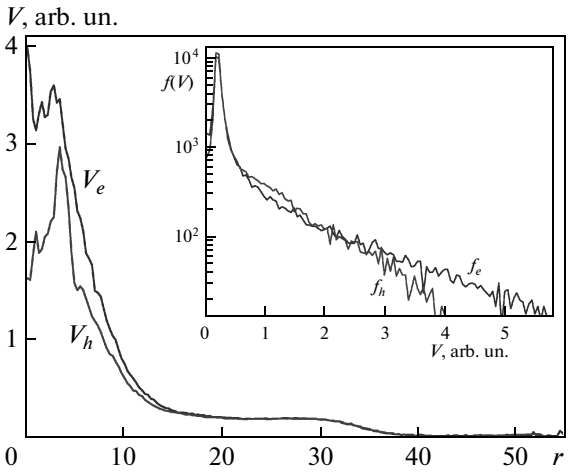

Fig. 10. Dependence of the electron (V_e) and hole (V_h) stream velocities on the distance r from the excitation spot center. The carrier velocities within the excitation spot region essentially exceed the maximal initial velocity ($= 1$). We note that V_e and V_h are the velocities of the part of the carriers that are below the optical phonon emission threshold. Inset: The electron ($f_e(V)$) and hole ($f_h(V)$) distributions over single-particle velocities. Parameters of the simulation are the same as in Fig. 9

means that most of the carriers escape from the spot very fast. This can be understood by estimating the critical number of carriers in the spot required for dominant in-layer repulsion (see Sec. 2): taking $n_c \sim d^{-2}$, we obtain $N_c = n_c \pi r_0^2 \sim \pi \left(r_0/d\right)^2 \approx 30$, which is much smaller than the above number of carriers formed in the spot during the unit time. (For the estimate, we have used the parameters in the caption to Fig. 9.) The system of charge carriers is therefore in the critical state.

The mechanism of the ring pattern formation in these conditions is as follows. The internal ring is formed due to the carriers that have emitted optical phonons. This can be seen in Fig. 10 by the sharp changes of carrier velocities within the excitation spot. We note that the velocities essentially exceed the maximal initial velocities there. (In addition, the optical phonon emissions were seen during the simulations by changes of instant maximal velocities of the carriers that were up to the threshold velocity of optical phonon emission.) This means that the in-layer repulsive Coulomb interaction is dominant in the excitation spot. The repulsive forces accelerate the carriers in such a way that the major part of them emits optical phonons and then quickly forms excitons. The carriers with velocities beneath the threshold velocity of optical phonon emission go further emitting acoustic phonons and, eventually, form excitons relatively far away from the excitation spot. This description is in excellent agreement with all sets of simulations in the MGR, and it therefore justifies the second scenario suggested in Sec. 2. Some details of the Coulomb repulsion accompanied by phonon emission are given in Appendix B.

To prove the crucial role of Coulomb interactions, we have performed a simulation where the interactions

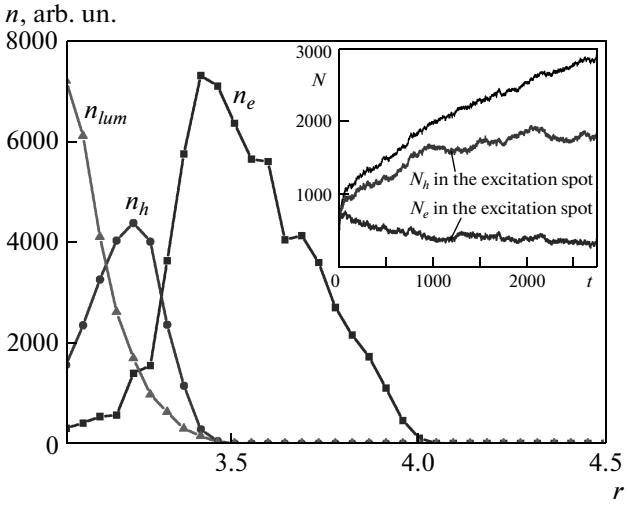

Fig. 11. In-layer distributions of electrons (n_e), holes (n_h), and luminescence ($n_{lum}(r)$) averaged over the time interval $(1500, 2700)$ in the absence of any direct Coulomb interactions. Inset: the dependence of the total number N of electrons and holes on time t. It shows that the dynamics is still non-stationary. Parameters of the simulation are the same as in Fig. 9

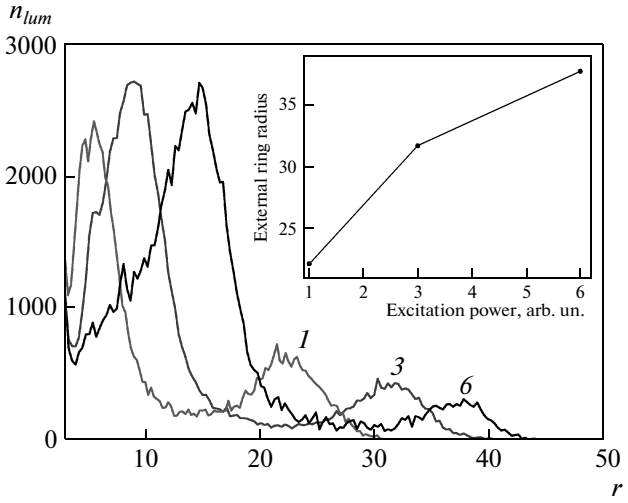

Fig. 12. Dependence of the stationary in-layer luminescence distribution $n_{lum}(r)$ on the excitation power with the number ΔN_{spot} of particles generated per time step in the spot shown by numbers (1, 3, 6) near the corresponding curves. Inset: dependence of the external ring radius on the excitation power. The other parameters of the simulations are the same as in Fig. 9

are switched off, even though the exciton formation condition holds. The results are shown in Fig. 11. We see that the saturation of $N(t)$ (i. e., the stationary state) is absent during the time that essentially exceeds previous simulation times for the MGR. The in-layer distributions of electrons and holes resemble those for the "first way" SGR, i. e., the distributions are spatially separated. However, the ring does not form and the luminescence decreases monotonically from the center.

We now discuss the dependence of the ring-shaped pattern on the pumping power and the critical relative velocity V_c from the exciton formation condition.

The dependence of in-plane positions of the rings on the pumping rate is shown in Fig. 12. The external ring radius increases nearly linearly, whereas the internal ring radius increases more slowly. This behaviour exhibits a good agreement with the experimental curves (Fig. 2). (Determining the dependences more accurately requires collecting larger statistics that is a very time-consuming procedure due to the large total numbers ($\sim 10^4$) of particles in the MGR.)

The dependence of the ring-shaped luminescence pattern on the critical relative velocity V_c shows (Fig. 13) that the smaller V_c is, the larger the external ring radius (the top inset in Fig. 13) and the ring intensity. At the same time, the stationary number of carriers increases to the limiting values of the order

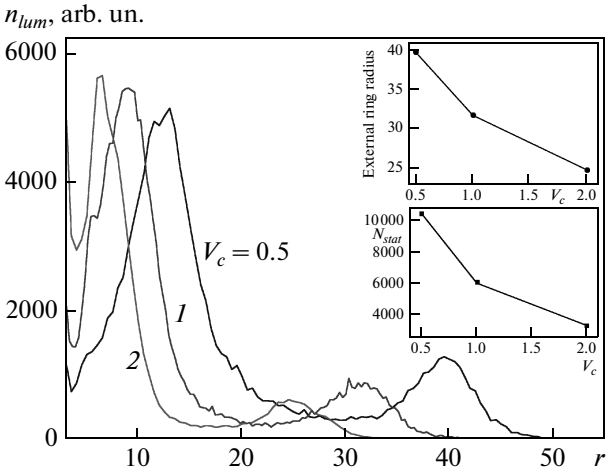

Fig. 13. Dependence of the stationary in-layer luminescence distribution $n_{lum}(r)$ on the critical relative velocity V_c from the exciton formation condition. Top inset: dependence of the external ring radius on V_c. Bottom inset: the stationary total number N_{stat} of carriers vs V_c. The pumping rate $\Delta N_{spot} = 3$. The other parameters of the simulations are the same as in Fig. 9

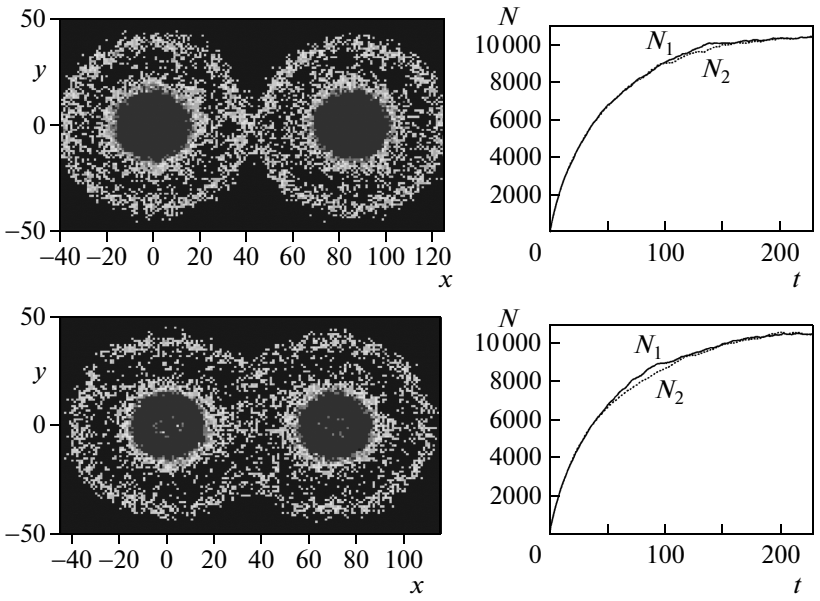

Fig. 14. Left: Luminescence patterns in the case of two excitation spots at two distances, 85 (top) and 70 (bottom), between the spot centers. Right: The corresponding dependences of the total numbers $N_{1,2}$ of carriers excited by the spots on time t show that the system arrives at the stationary state. Parameters of the simulations are the same as in Fig. 9 except the critical relative velocity, here $V_c = 0.5$

of 10^4 (the bottom inset in Fig. 13) for the available computational power.

Finally, we have performed simulations with two identical but spatially separated excitation spots to compare our results (see Fig. 14) with experimental pictures [13, 30]. In can be seen that when the spots are placed close enough, the external rings open towards each other, forming a figure similar to one of the Cassini ovals. This behavior also corresponds to the experiments, even though the simulations do not include the exciton dynamics.

Summarizing the simulation results for the MGR, we conclude that they show reasonable correspondence with the experiments [6, 13, 24, 30]. Therefore, the theoretical explanations [13, 14, 16–18, 24] of the ring pattern formation based on the diffusion-induced spatial separation of in-layer distributions of electrons and holes (see Appendix A) must be revised.

5. CONCLUSION AND DISCUSSION

It has been shown that the stationary ring-shaped luminescence pattern forms due to the hot carrier transport (HCT) caused by the in-plane electric fields which appear at high enough excitation power in the excitation spot region. The HCT is essentially non-diffusive. In particular, the internal luminescence ring appears due to the electrons and holes emitting optical phonons, whereas the external ring forms due to the relaxation of the carriers that are initially below the optical phonon emission threshold. To form excitons, these carriers relax emitting acoustic phonons and, in addition, due to the interlayer Coulomb drag.

The ring-shaped pattern formation is particularly interesting as a possible bright signature of self-organized criticality [28, 31]. Although the "second scenario" naturally involves the SOC regime, the MGR simulations reported have been performed in the critical state. Thus, the transition to the SOC regime as well as its statistical properties (e. g., $1/f$-noise) in this system are still open questions.

The author thanks L. P. Paraskevova and L. I. Kondrashova for the encouragement, and Yu. M. Kagan and F. V. Kusmartsev for the helpful discussions.

APPENDIX A

Diffusive model of charge carrier transport

The diffusive transport model [13] used to explain the experiments [6] was based on two reaction-diffusion equations

$$\dot{n}_e = D_e \nabla^2 n_e - w n_e n_h + J_e(r), \quad (8)$$

$$\dot{n}_h = D_h \nabla^2 n_h - w n_e n_h + J_h(r), \quad (9)$$

where n_e and n_h are electron and hole $2D$ densities and w is electron–hole binding rate to form an exciton. The source term $J_h(r) = P_{ex}\delta(\mathbf{r})$ for photoexcited holes is focused in the local excitation spot. The density of photoexcited electrons is supposed to be negligible in comparison with the equilibrium electron density n_∞ in the absence of laser excitation. When n_∞ is spatially disturbed due to the presence of holes, there appears the electron current $J_e(r) = I - a n_e(r)$, which is spread in the quantum-well plane. Here, I and $a n_e$ are the currents in and out of the system, respectively, such that $n_\infty = I/a$. (We note that a here is not the critical relative distance used in the simulations but an independent parameter.) Implying the stationary regime and the symmetry with respect to the polar angle, and neglecting the exciton diffusion [15], one obtains the exciton PL intensity $I_{PL}(r) \propto n_e(r) n_h(r)$.

The authors of Ref. [13] have assumed that a luminescence ring with radius R appears at the overlap of the electron and hole densities (see Fig. 15) so that $n_h \gg n_e$ at $r < R$ and $n_h \ll n_e$ at $r > R$ with $n_e(r \to \infty) = n_\infty$ (Fig. 15). Neglecting the exciton formation term $w n_e n_h$ far from the boundary $r = R$, we obtain

$$\nabla^2 n_h \equiv \frac{d^2 n_h}{dr^2} + \frac{1}{r}\frac{dn_h}{dr} = -\frac{P_{ex}}{D_h}\delta(\mathbf{r}) \quad (10)$$

for holes. Using the boundary condition $n_h(r = R) = 0$ results in

$$n_h(r \le R) = \frac{P_{ex}}{2\pi D_h} \ln\frac{R}{r}. \quad (11)$$

Accordingly, for electrons one obtains

$$\nabla^2 n_e = -(I/D_e) + (a/D_e)\, n_e(r)$$

with boundary conditions $n_e(r = R) = 0$, $n_e(r \to \infty) = n_\infty$.

Denoting $\Delta = (n_e - n_\infty)/n_\infty$ and $x = r/\lambda$, where $\lambda \equiv \sqrt{D_e/a} = \sqrt{D_e n_\infty / I}$ is a characteristic length, we arrive at

$$\frac{d^2\Delta}{dx^2} + \frac{1}{x}\frac{d\Delta}{dx} - \Delta = 0. \quad (12)$$

The last equation is the modified Bessel equation of zero order. The solution is

$$\Delta(x) = A K_0(x), \quad (13)$$

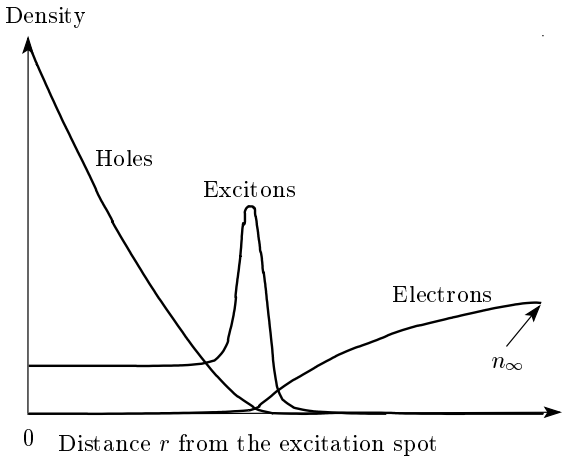

Fig. 15. The density distributions obtained in Ref. [13] with the use of the diffusive transport model

where A is a constant and $K_0(x)$ is the zero-order modified Hankel (or MacDonald) function, such that

$$K_0(x \to 0) \approx \ln\frac{1}{x}, \quad K_0(x \to \infty) = 0.$$

Hence,

$$n_e(r)/n_\infty = 1 + A K_0(r/\lambda). \quad (14)$$

If $\lambda \gg R$, as supposed in [13], then the electron density $n_e(r)/n_\infty \approx 1 + A\ln(\lambda/r)$ at $R < r \ll \lambda$. Using the boundary condition $n_e(r = R) = 0$, we find the coefficient A. Finally,

$$n_e(R < r \ll \lambda) \approx n_\infty \left[1 - \frac{\ln(\lambda/r)}{\ln(\lambda/R)}\right]. \quad (15)$$

Then it has been assumed that at the boundary between the electron and hole densities the total current is zero, i. e.,

$$D_e \left.\frac{\partial n_e}{\partial r}\right|_{r=R} = -D_h \left.\frac{\partial n_h}{\partial r}\right|_{r=R}. \quad (16)$$

From Eq. (16) it follows that

$$\frac{D_e n_\infty}{\ln(\lambda/R)} = \frac{P_{ex}}{2\pi}, \quad (17)$$

and therefore the ring radius can be expressed as

$$R = \lambda \exp(-2\pi D_e n_\infty / P_{ex}). \quad (18)$$

If we set $D_h = 0$, then the ring radius R must be equal to zero because, according to the model [13], the diffusion of holes is the only reason why they move out of the excitation spot. But Eq. (18) does not depend on

D_h, and hence the ring radius is not zero at $D_h = 0$, i. e., the ring exists even if all holes are left in the excitation spot. This clearly unphysical result is not a consequence of the limit case $\lambda \gg R$, but rather comes from wrong initial assumptions. (In Ref. [17], the result, Eq. (18), has been generalized but even then R does not depend on D_h.)

We note that in the original paper [13], the erroneous formula for R has been given [27]

$$R_{orig} = \lambda \exp\left(-\frac{2\pi D_e n_\infty}{D_h P_{ex}}\right). \tag{19}$$

The presence of D_h in the exponent denominator could be deceiving because at first sight (i. e., without the dimensionality check: $[D_e] = [D_h] = \text{cm}^2/\text{s}$, $[n_\infty] = \text{cm}^{-2}$, $[P_{ex}] = \text{s}^{-1}$) it looks reasonable.

In addition, both the DTM [13] and its modifications [14, 16–18] could not explain in principle why the external luminescence ring appears only when the excitation power exceeds some critical value.

Nevertheless, the drift-diffusion regime can be applicable for slow charge carriers near the luminescence ring at $r \sim R$. (As before, we do not consider equilibrium carriers and are only focused on photogenerated ones.) In particular, the continuity equations in this regime are given by

$$\dot{n}_{e(h)} + \operatorname{div} \mathbf{i}_{e(h)} = g_{e(h)} - \Gamma, \tag{20}$$

$$\dot{n}_X + \operatorname{div} \mathbf{i}_X = \Gamma - n_X/\tau_X. \tag{21}$$

Here n_e, n_h and $\mathbf{i}_e = -n_e\mu_e\mathbf{E} - D_e\nabla n_e$, $\mathbf{i}_h = n_h\mu_h\mathbf{E} - D_h\nabla n_h$ are $2D$ densities and particle flux densities of uncoupled electrons in the plane $z = d/2$ and holes in the plane $z = -d/2$, and $\mu_{e(h)}$ is the electron (hole) mobility. The particle flux density for excitons is $\mathbf{i}_X \approx -D_X\nabla n_X$, where n_X is the interlayer exciton density. The contribution from the dipole–dipole interaction between the excitons is omitted in $\mathbf{i}_X$ because it appears as an above-linear correction on n_X. The carrier generation rates $g_{e(h)}(\mathbf{r}, t)$ are some given functions. The exciton formation rate can be written as (inessential constant prefactors are dropped hereafter)

$$\Gamma(\mathbf{r}, t) = \int w(|\mathbf{v}_1 - \mathbf{v}_2|) \times \\ \times f_e(\mathbf{r}, \mathbf{v}_1, t)\, f_h(\mathbf{r}, \mathbf{v}_2, t)\, d^2\mathbf{v}_1 d^2\mathbf{v}_2, \tag{22}$$

where $f_{e(h)}(\mathbf{r}, \mathbf{v}, t)$ is the electron (hole) distribution function, such that

$$n_{e(h)}(r, t) = \int f_{e(h)}(r, \mathbf{v}, t)\, d^2\mathbf{v},$$

and $w(v)$ is the specific exciton formation rate. The exciton lifetime τ_X is supposed to be density independent. Finally, the Poisson equation for the electric field is given by (time dependence is dropped; ϵ is the dielectric constant)

$$\operatorname{div}(\epsilon\mathbf{E}(r, z)) = 4\pi e[(n_h(r) + n_X(r))\,\delta(z + d/2) - \\ - (n_e(r) + n_X(r))\,\delta(z - d/2)]. \tag{23}$$

It includes the contribution of the interlayer exciton dipole fields and keeps the electroneutrality for the free carrier system when the exciton formation is suppressed ($n_X(r) = 0$).

At $r \sim R$, one can set $w(v) \approx w_{max}$, then $\Gamma(r) \approx \approx w_{max} n_e(r)\, n_h(r)$ and Eqs. (20), (21), and (23) with $g_{e(h)} = 0$ become a closed system.

We note that the ambipolar electric field $\mathbf{E}$ might play an important role in the formation of a sharp intensity profile of the external luminescence ring. In this regard, it is useful to note that the FWHM of the external ring intensity is almost independent of the ring radius R at high excitation powers (see Fig. 2).

APPENDIX B

If $e^2\sqrt{n} > \hbar\omega_{opt}$ at $n > d^{-2}$, then the in-layer Coulomb repulsion in the excitation spot might be "exhausted" at small distances: the potential energy of the carriers transforms into kinetic energy, which, in turn, is spent on the fast optical phonon emission so that the carriers do not go far from the excitation spot.

To estimate whether the values of carrier densities in the excitation spot are sufficient for such process, we consider two electrons resting at distance r_0 from each other at the moment $t = 0$. We neglect the energy dissipation due to acoustic phonon emission first, to facilitate the effect described above. Then the equation of motion is

$$m\ddot{r} = e^2/r^2,$$

with $m = m_e^*/2$ and $r = |\mathbf{r}_1 - \mathbf{r}_2|$. (The dielectric constant ϵ is introduced by substituting $e^2 \to e^2/\epsilon$ in the final expression.) The solution is expressed through the inverse function,

$$t/t_0 = \sqrt{x^2 - x} + \frac{1}{2}\ln\left(x + \sqrt{x^2 - x}\right),$$

where $x = r/r_0$ and $t_0 = \sqrt{mr_0^3/2e^2}$. At $t > (3 \div 4)t_0$, with a good precision, the velocity is $v \approx v_\infty = r_0/t_0$, i. e., the electrons move nearly uniformly at large times. The condition of optical phonon emission is given by

$$\frac{mv^2}{2} = \frac{e^2}{r_0} - \frac{e^2}{r} \geq \hbar\omega_{opt},$$

whence it follows that

$$r \geq r_c = \frac{r_0}{1 - \hbar\omega_{opt}/\left(e^2/r_0\right)}.$$

Substituting $r_0 \sim n^{-1/2}$ in the expression for r_c gives

$$n \sim \left(\epsilon\hbar\omega_{opt}/e^2 + 1/r_c\right)^2.$$

The value $n_c^* = \left(\epsilon\hbar\omega_{opt}/e^2\right)^2 \approx 4 \cdot 10^{13}$ cm^{-2} (with $\epsilon \approx 12.8$ and $\hbar\omega_{opt} \approx 37$ meV for GaAs) at $r_c = \infty$ is the smallest density at which the process of optical phonon emission is dominant. We note that at $n > n_c^*$ the effect is extremely pronounced, e. g., $r_c \approx 1$ μm at $n = 1.003 n_c^*$ (extra 0.3 % to n_c^*). At $n = n_c^*$, we obtain $r_0 \sim 0.1 a_B$ for GaAs.

To find a qualitative dependence of the carrier flux velocity on in-plane coordinates when the carrier kinetic energies are below the optical phonon emission threshold, we consider the previous model adding the dissipation due to acoustic phonons. Then for two electrons we have (unit vectors are dropped)

$$m_e^* \ddot{\mathbf{r}}_1 = e^2/\left|\mathbf{r}_1 - \mathbf{r}_2\right|^2 - \gamma\dot{\mathbf{r}}_1,$$
$$m_e^* \ddot{\mathbf{r}}_2 = -e^2/\left|\mathbf{r}_1 - \mathbf{r}_2\right|^2 - \gamma\dot{\mathbf{r}}_2,$$

where $\gamma = e/\mu_e$ is the dissipation coefficient and μ_e is the electron mobility. Substituting $\mathbf{R} = \left(\mathbf{r}_1 + \mathbf{r}_2\right)/2$ and $\mathbf{r} = \mathbf{r}_1 - \mathbf{r}_2$, in the center-of-mass frame ($\dot{\mathbf{R}} = 0$), we obtain the equation of motion

$$m\ddot{r} = \frac{e^2}{r^2} - \frac{1}{2}\gamma\dot{r}.$$

Dissipation of the energy $E(r) = mv^2(r)/2 + e^2/r$ is given by $dE/dr = -\gamma v(r)/2$ (because $dE/dt = -\gamma v^2/2$), which leads to the equation

$$mv(r)\frac{dv}{dr} = \frac{e^2}{r^2} - \frac{1}{2}\gamma v(r).$$

In the dimensionless form ($r = r_0 x$, $v = v_\infty u$), we have

$$u(x)\left[\frac{du}{dx} + a\right] = \frac{1}{2x^2}, \qquad (24)$$

where $a = \sqrt{\gamma^2 r_0^3/8me^2}$, $x \geq 1$, and $u(x = 1) = 0$. (To avoid a confusion, we note again that this a has its own meaning.) Using the relation $\gamma = e/\mu_e$, we can rewrite the parameter as $a = (1/2)\left(r_0/\xi_e\right)^{3/2}$, where $\xi_e = \sqrt[3]{m_e^* \mu_e^2}$ is the characteristic length scale. Taking $\xi_e \sim 1$ μm for GaAs (see the description of the numerical model in the main text) and $r_0 \sim n_c^{-1/2} \sim$ $\sim d \sim 10^{-6}$ cm, we obtain $a \sim 10^{-3}$. Equation (24) can be reduced to the Abel equation of the second kind. Its

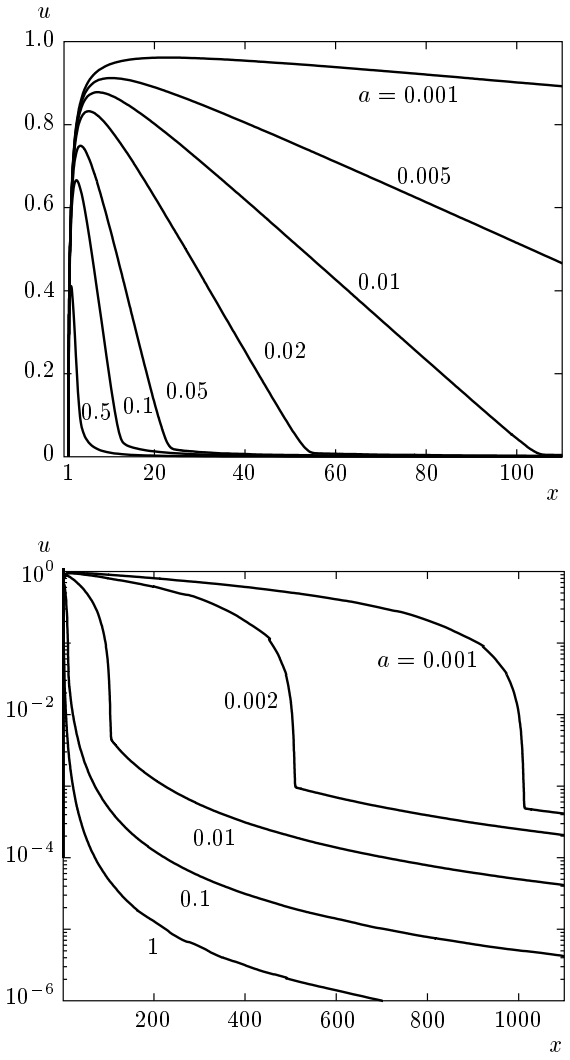

Fig. 16. Numerical solutions of Eq. (24) with $u(x) = v/v_\infty$ and $x = r/r_0$ for different values of the parameter a. Top: Linear scale. Bottom: Log scale

exact analytical solution is unknown. However, a qualitative behavior of $u(x)$ can be found from the asymptotic solutions at $x \to 1$ and $x \to \infty$ (see also numerical solutions in Fig. 16). It is natural to assume that velocity $u(x = \infty) = 0$. Hence, du/dx can be dropped in Eq. (24) at $x \to \infty$ that gives $u_\infty(x) \approx (2ax^2)^{-1}$. We now rewrite Eq. (24) as

$$\frac{du}{dx} = \frac{1}{2x^2 u} - a.$$

At $x \to 1$, due to the initial condition $u \to 0$ and therefore the last term in the right-hand side can be dropped. This gives $u_1(x) \approx \sqrt{1 - 1/x}$ at $x \approx 1$. The dependence of $u(x)$ on a is as follows: the larger a is, the narrower the width of the peak and the smaller its

height (see Fig. 16). We note that in the laboratory frame $v_{e,h} = v/2$ and $r_{e,h} = r/2$.

It is also interesting to note that the MGR simulations indicate that the external luminescence ring appears only if the carrier stream velocities $V_{e(h)}(r)$ as functions of the distance r from the excitation spot (see Fig. 10) have a non-monotonic dependence similar to that in Fig. 16, i. e., the velocities increase at small r, reaching the maximal values at some finite r (often within the excitation spot region), and then decrease to zero at large r.

APPENDIX C

Suppression of exciton formation in the bilayer at high e–h relative velocity

Here, we illustrate how the critical relative velocity V_c appears in principle in the exciton formation condition. We can distinguish two mechanisms referred to in what follows as "geometric" and "kinetic" ones, which lead to the existence of the critical e–h relative velocity above which the interlayer exciton formation is strongly suppressed.

1. "Geometric" mechanism. Due to the bilayer geometry, at sufficiently large relative e–h velocity the interlayer Coulomb attraction, which results in an exciton formation, is suppressed. To show this, we consider the Fourier transform

$$U_q = \int d^2\mathbf{r} \exp(i\mathbf{q}\cdot\mathbf{r})\, U(r)$$

of the pair interaction potential

$$U(r) = -e^2/\sqrt{r^2+d^2}$$

between an electron from one layer and a hole from another (r is the in-plane relative distance). We obtain

$$U_q = -2\pi e^2 \int_0^\infty \frac{J_0(qr)\, r\, dr}{\sqrt{r^2+d^2}} = -\frac{2\pi e^2}{q}\exp(-qd), \quad (25)$$

the "screened Coulomb potential" in the momentum space. (The effects of charge screening studied in the random phase approximation [37] lead to a change in the preexponential factor, which is not important in this consideration.) Hence, if the electron–hole relative velocity

$$V = \frac{\hbar q}{m} > V_c = \frac{\hbar}{md},$$

then the interaction between the carriers decreases exponentially as V increases. This means that we can neglect the interaction as well as the exciton formation at $V > V_c$. At $d \approx 10^{-6}$ cm [29] and the reduced e–h mass $m \approx 0.06m_e$ in GaAs, we obtain $V_c \approx 3\cdot 10^7$ cm/s, which is of the same order of magnitude as the threshold velocity v_{max} of optical phonon emission in GaAs ($v_{max}/V_c \approx 1.5$).

2. "Kinetic" mechanism. The second mechanism is based on the fact that to form an exciton, the unbound electron–hole pair must emit an acoustic phonon. (Here, we suppose that the carrier velocities are below the optical phonon emission threshold.)

To illustrate this, we consider a model system: an infinite train of electrons separated from each other by distance L uniformly moves with velocity V along a thread and an immovable hole is located at distance d from the thread. The interaction potential between the electron train and the hole as a function of time is given by

$$U(t) = -\sum_{k=-\infty}^{\infty} \frac{e^2}{\rho_k},$$

where

$$\rho_k = \sqrt{(kL+Vt)^2 + d^2}.$$

Although the sum diverges as $1/|k|$, the relative value of the potential $\delta U(t) = U(t) - U(0)$ is convergent. The components of the corresponding force acting on the hole along and perpendicular to the thread are given by

$$F_\parallel(t) = \sum_{k=-\infty}^{\infty} \frac{e^2(kL+Vt)}{\rho_k^3}, \quad F_\perp(t) = \sum_{k=-\infty}^{\infty} \frac{e^2 d}{\rho_k^3}.$$

Both the potential and the force are periodic functions of time with the period $T = L/V$.

In the $2D$ case, when there exists relative flow (with velocity V) of electrons in one layer and holes in another, the interlayer interaction potential between the electron flow and a given hole oscillates with the frequency $\omega \sim V\sqrt{n}$, where n is the $2D$ density of electrons in the flow. If this frequency is higher than τ^{-1}, where $\tau = \min(\tau_{e-ac}, \tau_{h-ac})$ is the minimal carrier–acoustic phonon scattering time, the exciton formation in real space is not possible. We can therefore write the exciton formation condition as

$$V < V_c \sim 1/\sqrt{n\tau^2}. \quad (26)$$

If the carrier densities are essentially different, one should take $n = \max(n_e, n_h)$ in (26). At $n \sim 10^{10}$ cm^{-2} and $\tau \sim 10^{-9}$ s, the critical relative velocity is $V_c \sim \sim 10^4$ cm/s.

In fact, one can obtain the estimate (26) in a more simple way. We suppose for definiteness that locally $n_e > n_h$. Then an e–h pair with relative velocity V can form an exciton if

$$V\tau < \bar{r}_{e-e} \sim n_e^{-1/2},$$

that is, the electron or the hole should have time to emit an acoustic phonon before the next electron would come to the hole. The condition (26) follows directly from the last formula.

REFERENCES

1. S. A. Moskalenko, Sov. Phys. Sol. St. **4**, 199 (1962).
2. L. V. Keldysh and A. N. Kozlov, Sov. Phys. JETP **27**, 521 (1968).
3. T. Fukuzawa, E. E. Mendez, and J. M. Hong, Phys. Rev. Lett. **64**, 3066 (1990).
4. L. V. Butov et al., Phys. Rev. Lett. **73**, 304 (1994).
5. Yu. E. Lozovik and O. L. Berman, Zh. Eksp. Teor. Fiz. **111**, 1879 (1997).
6. L. V. Butov, A. C. Gossard, and D. S. Chemla, Nature **418**, 751 (2002).
7. D. Snoke et al., Nature **418**, 754 (2002).
8. A. V. Larionov and V. B. Timofeev, Pis'ma v Zh. Eksp. Teor. Fiz. **73**, 341 (2001).
9. A. V. Larionov et al., Pis'ma v Zh. Eksp. Teor. Fiz. **75**, 689 (2002).
10. D. Snoke et al., Sol. St. Commun. **127**, 187 (2003).
11. J. P. Eisenstein and A. H. MacDonald, Nature **432**, 691 (2004).
12. A. V. Balatsky, Y. N. Joglekar, and P. B. Littlewood, Phys. Rev. Lett. **93**, 266801 (2004).
13. L. V. Butov et al. Phys. Rev. Lett. **92**, 117404 (2004).
14. R. Rapaport et al., Phys. Rev. Lett. **92**, 117405 (2004).
15. L. S. Levitov, B. D. Simons, and L. V. Butov, Phys. Rev. Lett. **94**, 176404 (2005).
16. S. Denev, S. H. Simon, and D. W. Snoke, Sol. St. Commun. **134**, 59 (2005).
17. M. Haque, Phys. Rev. E **73**, 066207 (2006).
18. A. A. Chernyuk and V. I. Sugakov, Phys. Rev. B **74**, 085303 (2006).
19. M. H. Szymanska, J. Keeling, and P. B. Littlewood, Phys. Rev. Lett. **96**, 230602 (2006).
20. V. B. Timofeev and A. V. Gorbunov, J. Appl. Phys. **101**, 081708 (2007).
21. Sen Yang et al., Phys. Rev. B **75**, 033311 (2007).
22. M. Stern et al., Phys. Rev. Lett. **101**, 257402 (2008).
23. J. Kasprzak et al., Nature **443**, 409 (2006).
24. Sen Yang et al., Phys. Rev. B **81**, 115320 (2010).
25. A. V. Paraskevov and S. E. Savel'ev, Phys. Rev. B **81**, 193403 (2010).
26. H. Deng, H. Haug, and Y. Yamamoto, Rev. Mod. Phys. **82**, 1489 (2010).
27. A. V. Paraskevov, arXiv:0902.3909.
28. P. Bak, C. Tang, and K. Wiesenfeld, Phys. Rev. A **38**, 364 (1988).
29. L. V. Butov, J. Phys.: Condens. Matter **16**, R1577 (2004).
30. L. V. Butov et al., arXiv:cond-mat/0308117.
31. P. Bak, *How Nature Works: The Science of Self-organized Criticality*, Springer, New York (1996).
32. H. L. Stormer et al., Phys. Rev. B **41**, 1278 (1990).
33. M. P. Lilly et al., Phys. Rev. Lett. **90**, 056806 (2003).
34. H. P. van der Meulen et al., Phys. Rev. B **60**, 4897 (1999).
35. G. R. Facer et al., Phys. Rev. B **59**, 4622 (1999).
36. A. V. Paraskevov and S. E. Savel'ev, Phys. Rev. B **82**, 119902(E) (2010).
37. U. Sivan, P. M. Solomon, and H. Shtrikman, Phys. Rev. Lett. **68**, 1196 (1992).